nature energy

ARTICLES

PUBLISHED: 25 JANUARY 2016 | ARTICLE NUMBER: 15029 | DOI: 10.1038/NENERGY.2015.29

# Growth of conformal graphene cages on micrometre-sized silicon particles as stable battery anodes

Yuzhang Li[1†], Kai Yan[1†], Hyun-Wook Lee[1], Zhenda Lu[1], Nian Liu[2] and Yi Cui[1,3*]

**Nanostructuring has been shown to be fruitful in addressing the problems of high-capacity Si anodes. However, issues with the high cost and poor Coulombic efficiencies of nanostructured Si still need to be resolved. Si microparticles are a low-cost alternative but, unlike Si nanoparticles, suffer from unavoidable particle fracture during electrochemical cycling, thus making stable cycling in a real battery impractical. Here we introduce a method to encapsulate Si microparticles (~1–3 μm) using conformally synthesized cages of multilayered graphene. The graphene cage acts as a mechanically strong and flexible buffer during deep galvanostatic cycling, allowing the microparticles to expand and fracture within the cage while retaining electrical connectivity on both the particle and electrode level. Furthermore, the chemically inert graphene cage forms a stable solid electrolyte interface, minimizing irreversible consumption of lithium ions and rapidly increasing the Coulombic efficiency in the early cycles. We show that even in a full-cell electrochemical test, for which the requirements of stable cycling are stringent, stable cycling (100 cycles; 90% capacity retention) is achieved with the graphene-caged Si microparticles.**

Rechargeable lithium-based batteries with high energy density have been the subject of intense research to meet the ever-growing demands of portable electronics and electrical vehicles[1–3]. A variety of emerging anode and cathode materials has attracted much attention, including Si, Sn and Li metal for anodes[4–7], and S and $O_2$ for cathodes[8–11]. Among these materials, Si is an attractive anode material for next-generation lithium-ion batteries (LIBs; refs 12–14), having greater than ten times the theoretical capacity of commercial graphite anodes. However, challenges arise due to the large volume expansion of silicon (~300%) during battery operation, which causes mechanical fracture, loss of inter-particle electrical contact, and repeated chemical side reactions with the electrolyte.

To address these failure modes, a wide range of material design concepts have been developed following the initial insight of using one-dimensional Si nanowire structures[4]. First, mechanical fracture is avoided by decreasing the material feature size to the nanoscale with structures such as core–shell nanowires[15,16], hollow particles[17] and tubes[18], porous Si (refs 19–22), and Si–C composites[23–26]. Second, the powerful concept of an interior void space for volume expansion and a stable shell to prevent electrolyte infiltration was demonstrated in double-walled Si–$SiO_2$ hollow tubes[27] and further confirmed with the Si–C yolk-shell[28] and pomegranate structures[29]. In addition, new polymer binders, such as alginate[30], conducting polymers and hydrogels[31], and self-healing polymers[32] have been explored to improve Si anodes.

Despite these impressive advances in Si anodes, there remain two critical challenges to overcome: the heavy reliance on nanostructured Si for stable cycling and the poor first- and later-cycle Coulombic efficiencies. Although nanostructuring has been shown to improve cycling performance, Si nanomaterials are still costly and not yet scalable owing to their complex synthesis processes. Attempts to use Si microparticles (SiMP) as low-cost starting materials have showed some progress[32], although the cycling performance is still far from that of nano-Si owing to increased complications with particle fracture. Furthermore, the first-cycle Coulombic efficiency is typically in the range of 65–85%, far below that of commercial graphite anodes (90–94%). The later-cycle Coulombic efficiency is usually 98–99.7%, but still needs further improvement to 99.8–99.9% for practical battery applications. Recent work on pomegranate[29] and non-filling C–Si structures[22] show improvements in later-cycle Coulombic efficiency up to 99.87%, but requires hundreds of cycles to reach that value. The low Coulombic efficiencies of nano-Si are caused by the large surface area available to form a solid electrolyte interphase (SEI) and the irreversible trapping of Li by the dangling bonds of an amorphous carbon coating.

There are huge challenges associated with using low-cost, micrometre-sized Si source materials. Typically, Si particles larger than ~150 nm and Si nanowires larger than ~250 nm have been shown to fracture on lithiation[33–35]. During lithiation, SiMP (1–3 μm) would be broken into small nano-Si particles, losing electrical contact and increasing the surface area to form additional SEI (Fig. 1a). Here, we introduce the conformal growth of a conductive graphene cage as an ideal encapsulation material for stabilizing the previously non-functional SiMP during battery cycling (Fig. 1b). The conformal graphene cage completely surrounds the microparticle and imparts its attractive properties to Si, affording the following four advantages. First, despite particle fracture of SiMP, the mechanically strong and flexible graphene cage with a pre-engineered empty space remains undamaged and confines all the broken Si pieces within. When using a multilayered graphene cage, the gliding motion between individual graphene layers can facilitate the caging effect without breaking during SiMP volume expansion. Second, the essential electrical contact

[1]Department of Materials Science and Engineering, Stanford University, Stanford, California 94305, USA. [2]Department of Chemistry, Stanford University, Stanford, California 94305, USA. [3]Stanford Institute for Materials and Energy Sciences, SLAC National Accelerator Laboratory, 2575 Sand Hill Road, Menlo Park, California 94025, USA. [†]These authors contributed equally to this work. *e-mail: yicui@stanford.edu

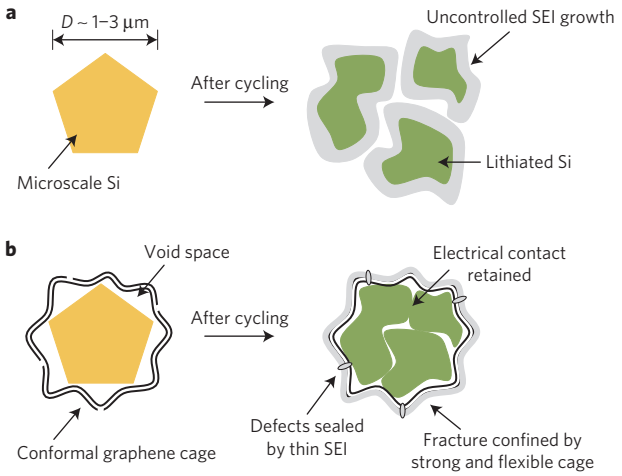


**Figure 1 | Design and structure of graphene cage encapsulation.** **a**, Si microparticles fracture and lose electrical contact during repeated battery cycling. Freshly exposed surfaces of Si continually react with the electrolyte, resulting in a thick and ionically insulating SEI layer. The destruction of electronic and ionic pathways leads to severe battery decay. **b**, The graphene cage imparts its mechanical strength, electrical conductivity and chemical stability to microscale Si, addressing the major challenges in its use. The mechanically flexible graphene cage confines the violent expansion and fracture of Si microparticles, while remaining undamaged to electrically connect the ruptured particles. Conductive additives are unnecessary even for thick electrodes (Supplementary Fig. 12) owing to the graphene cage's high electronic conductivity. Efficient SEI formation on the graphite-like surface of the graphene cage minimizes irreversible Li-ion loss, resulting in high initial- and later-cycle Coulombic efficiency and fast charge-transfer kinetics at the surface. These features enable stable cycling of Si microparticles even in full-cell configurations.

between fractured Si particles within each conducting graphene cage is preserved. Third, the graphene cage's intrinsically high electronic conductivity and ionic permeability through defects allows SiMPs and the resulting fractured particles to remain electrochemically active. Last, the SEI is expected to form mainly on the graphene cage and seal any possible defects to prevent electrolyte infiltration through the conformal shell. The surface chemistry of the graphene cage is similar to that of graphite, leveraging two decades of knowledge on the stable SEI formation on graphite[36–38] and resulting in high first- and later-cycle Coulombic efficiency. The graphene cage addresses both particle fracture and an unstable SEI, demonstrating excellent battery performance for microscale Si in a full-cell configuration (100 cycles; 90% retention).

## Synthesis and characterization of graphene cage

The graphene cage encapsulation must be highly conformal in order for Si to acquire the remarkable properties of graphene. Internal empty space is also necessary for Si expansion and fracture within the graphene cage. To this end, we have developed a unique and simple synthesis approach using a dual-purpose Ni template. The Ni serves as both the catalyst for graphene growth and the sacrificial layer for providing void space (Fig. 2a). Using electroless deposition[39], we conformally coat SiMPs with Ni, the thickness of which can be easily tuned for the appropriate void space. Next, a benign carburization process[40,41] activates the Ni-coated SiMP for low-temperature (450 °C) graphene growth through a dissolution-precipitation mechanism[42]. Last, we etch away the Ni catalyst using $FeCl_3$ aqueous solution, opening up the void space for SiMP expansion within the graphene cage (Fig. 2b,c and Supplementary Fig. 4). The multilayered structure of the graphene cage (~10 nm) is clearly observed from the transmission electron microscopy (TEM) image (Fig. 2d). Note that the cage exhibits a wavy structure due to conformal graphene growth along the large grains of Ni deposited onto the SiMP (Supplementary Fig. 2). The mechanically robust graphene cage remains continuous throughout the curved regions, which act as a buffer to accommodate acute interior stresses during particle fracture. Even after complete removal of Si by NaOH aqueous solution, the self-supporting graphene cage still remains structurally stable (Fig. 2e and Supplementary Fig. 6). Raman spectroscopy reveals the highly graphitic nature[43] of the cage as compared with amorphous carbon synthesized based on previous studies[29] (Fig. 2g). The pronounced D band with a narrow bandwidth suggests that sufficient defects are present to facilitate Li-ion transport to Si. Furthermore, the considerably screened Si peak (Fig. 2f) found using X-ray photoelectron spectroscopy (XPS) provides evidence for the conformal nature of the graphene cage, which makes up only 9% of the composite's total mass (Supplementary Fig. 5). With a lower carbon content, the graphene cage minimizes the possibility of irreversibly trapping Li ions without compromising the specific capacity of the composite.

## Electrical and mechanical behaviour of graphene cage

To substantiate the impressive characteristics of the graphene cage, we examined its electrical and mechanical behaviour on the single-particle level using a piezo-controlled, electrical biasing TEM-AFM holder. A circuit was built by sandwiching the graphene-encapsulated SiMP between a conducting Au substrate and a sharp W tip (Fig. 3a). Monitoring the live TEM image (Fig. 3b inset) ensured good electrical contact. By measuring the current as a function of applied voltage (Fig. 3b), we determined the electrical resistance of the graphene cage (~17 kΩ) to be a hundredfold less than that of an amorphous carbon coating (~1.4 MΩ) synthesized according to previous methods[29]. This is a remarkable result when considering the low-temperature synthesis of the graphene cage (450 °C) takes place at a lower temperature than that of the amorphous carbon (800 °C). The electrically conductive graphene-encapsulated SiMP can enable electrical connectivity even through thick electrodes constructed free of any conductive additives.

With the same experimental configuration, we can use the piezo-controllers to apply an external load onto empty shells of graphene and amorphous carbon, and observe their mechanical deformation *in situ*. From Fig. 3c and Supplementary Video 1, it is clear that the fragile amorphous carbon sphere cracks and breaks after only a slight deformation. This brittleness limits its ability to contain the violent particle fracture of microscale Si. In contrast, the graphene cage exhibits resilience to an external load (Fig. 3d and Supplementary Video 2) due to its superior mechanical strength and flexibility. Not only is the graphene cage able to fully collapse its shape during compression, it returns to its original structure completely intact after the load is removed. Coupled with its superb electrical conductivity, these distinct qualities of the graphene cage make it well suited to address silicon's failure modes during (de)lithiation.

## *In situ* lithiation of graphene-encapsulated SiMP

We reveal the lithiation process of the graphene-encapsulated SiMP *in situ*[44,45] by using a nanoscale electrochemical cell inside the TEM (Fig. 4a). These experiments allow us to directly observe silicon's intrinsic volume expansion and particle fracture during battery operation. From Fig. 4b and Supplementary Video 3, the SiMP apparently expands slowly until the particle finally fractures in a vigorous fashion. Despite the abrupt and violent rupture of the interior Si, the graphene cage clearly preserves its structural integrity throughout the process—unlike amorphous carbon, which has been shown to crack rather easily[29]. We note that the volume expansion is apparently highly anisotropic, indicative of crystalline silicon's tendency to favour expansion in certain crystallographic directions

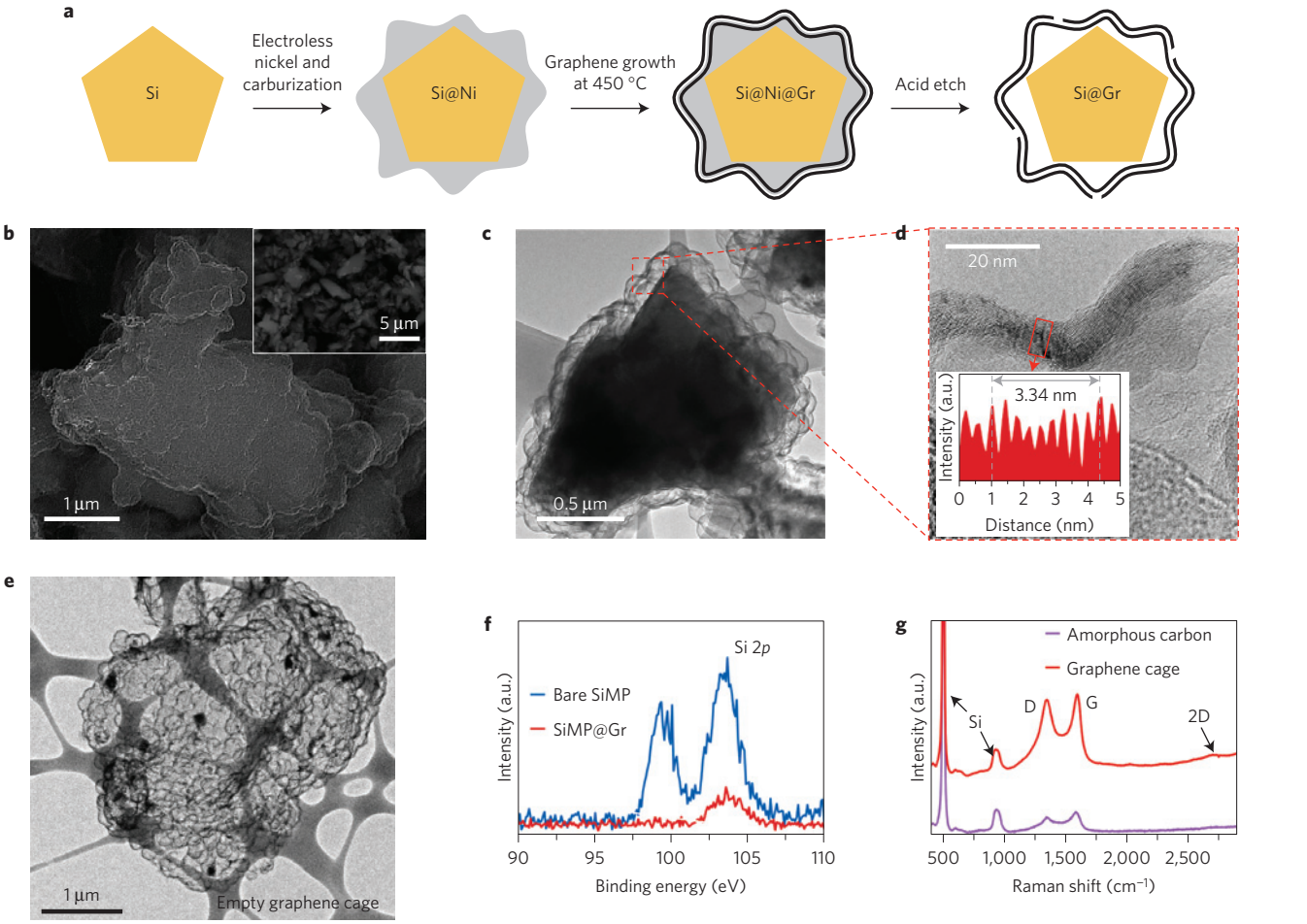


**Figure 2 | Synthesis and characterization of graphene cage structure. a**, Schematic of dual-purpose Ni template synthesis. **b**, SEM image of a graphene-encapsulated Si microparticle (SiMP@Gr). The inset gives a broader view, showing many Si microparticles encapsulated by the graphene cage. **c**, TEM image of an individual particle of SiMP@Gr. **d**, High-resolution TEM image of the graphene cage's layered structure. The intensity plot shows that ten layers span a distance of 3.34 nm (average inter-layer distance: 0.334 nm), a clear indication of graphene layers. **e**, TEM image of the hollow graphene cage after etching Si in NaOH. **f**, XPS spectra of Si 2*p* peaks of bare and graphene-encapsulated SiMP. The Si 2*p* peak is drastically decreased with the graphene cage indicating a conformal coating. **g**, Raman spectra of amorphous-carbon-coated (SiMP@aC) and graphene-encapsulated SiMP.

over others[34,35]. This anisotropic expansion is a primary reason why conventional secondary coatings are impractical for SiMP. A non-uniform void space would need to be exactly engineered along the specific crystallographic directions where expansion is favoured; otherwise, the rigid and fragile coating would break. Contrastingly, the graphene cage is shown to be mechanically strong and flexible. This allows it to survive the large interior stresses during microscale silicon's anisotropic expansion and particle fracture, while still retaining electrical contact between the fractured particles.

## Electrochemical performance

The favourable effects of the graphene cage on SiMP were verified by electrochemical tests in both half-cell and full-cell configurations. Type 2032 coin cells were constructed (see Methods) for deep galvanostatic cycling tests from 0.01 to 1 V (half cell) and 3.0 to 4.2 V (full cell). All reported capacities are based on the total mass of Si and C in the graphene cage composite.

The half-cell data in Fig. 5a show the reversible capacity of the graphene-encapsulated SiMP reached ~3,300 mAh $g^{-1}$ at a current density of C/20 (1C = 4.2 A $g^{-1}$). The high capacity indicates that the active materials are electrically well connected and participate fully in electrochemical lithiation and delithiation. Furthermore, this is achieved without the use of any conductive additives, exhibiting the excellent electrical conductivity of the graphene cage. From the 4th to 300th cycle, continued cycling at a higher rate of C/2 (1.5 mA $cm^{-2}$) resulted in capacity retention of over 85% for 300 cycles (Supplementary Fig. 7). After that, over 1,400 mAh $g^{-1}$ of capacity remained, which is still approximately four times that of graphite's theoretical capacity. This cycling stability and rate performance is the best as yet reported for microscale Si, and far surpasses that of bare or amorphous-carbon-coated SiMP (Fig. 5a).

We can attribute this cycling stability to the well-designed graphene cage structure. From the *ex situ* TEM images in Fig. 5d, it is clear that the graphene cage stays intact while the fractured microscale Si remains electrically connected on the particle level. Furthermore, cross-sectional scanning electron microscope (SEM) images show that the graphene cage's built-in void space prevents large changes in electrode thickness (only 11% change in thickness, Fig. 5b), allowing the fractured Si to maintain electrical contact on the electrode level. Without the caging feature of the graphene cage, bare Si microparticles quickly become electrically disconnected from each other, resulting in an unstable particle morphology, catastrophic electrode swelling by over 150%, and eventual disintegration (Fig. 5c).

We emphasize that, in addition to cycling stability, high Coulombic efficiencies are critical for the operation of a practical battery. Early-cycle Coulombic efficiencies are especially important because they account for most of the Li-ion loss and electrolyte

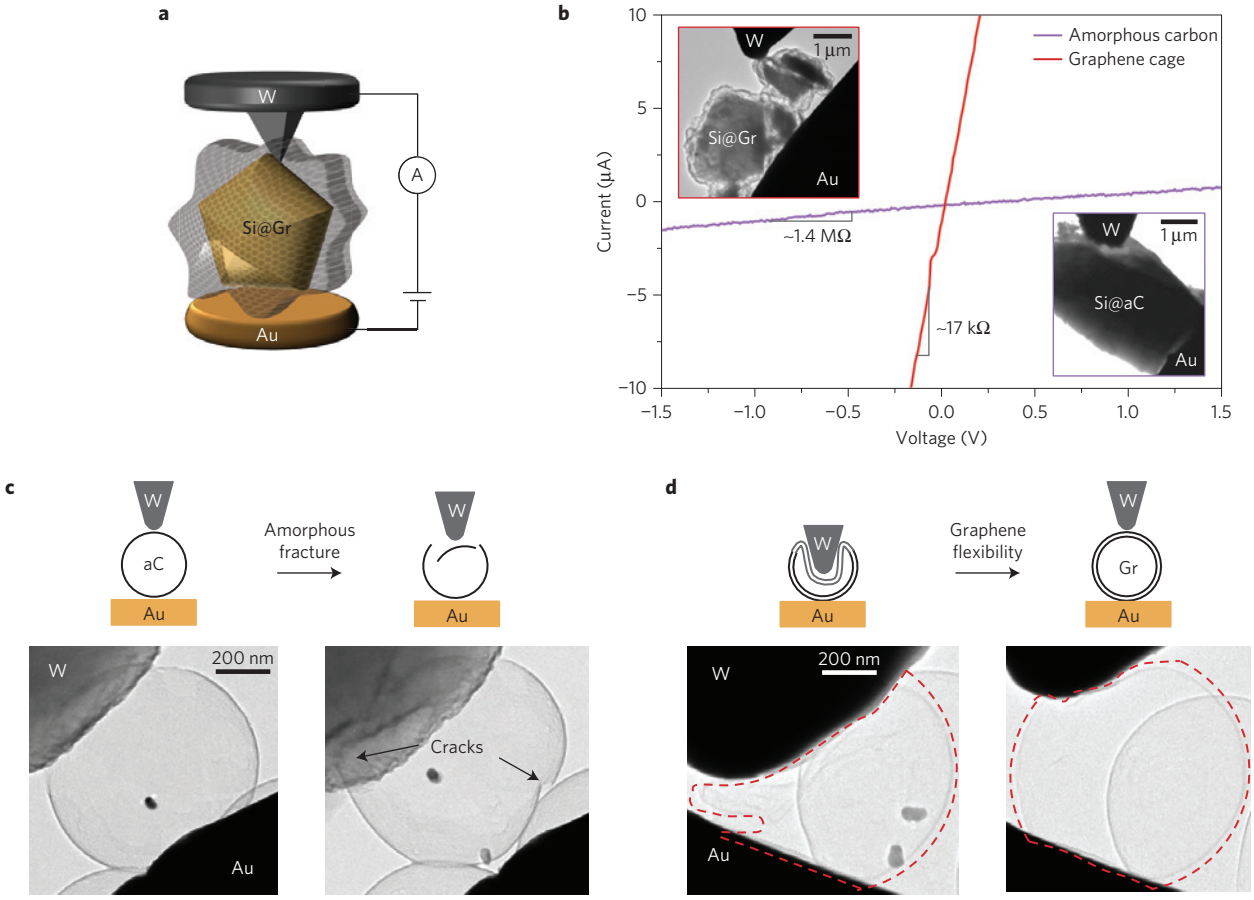


**Figure 3 | Particle-level characterization of graphene cage by *in situ* TEM. a**, Diagram of the electrical circuit for current–voltage measurements and external load testing. **b**, Current–voltage data of graphene-encapsulated and amorphous-carbon-coated SiMP. Insets are live TEM images of their respective contact positions: graphene cage in the red border and amorphous carbon coating in the purple border. The ohmic behaviour clearly shows that the graphene cage's electrical resistance (~17 kΩ) is a hundredfold less than that of the amorphous carbon coating (~1.4 MΩ). **c**, Schematic and time-lapse TEM images (Supplementary Video 1) of external load testing on empty shells of amorphous carbon. After only a slight deformation, the brittle amorphous carbon shell cracks, destroying the spherical structure. **d**, The graphene cage exhibits good flexibility during an external load (Supplementary Video 2). Its shape can be fully collapsed during compression and returns undamaged to its original structure after unloading.

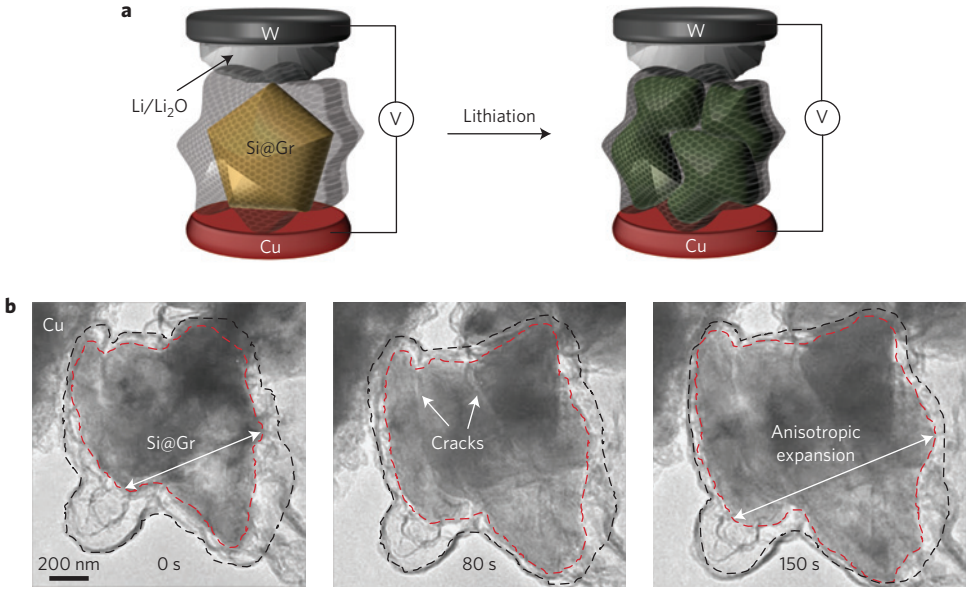


**Figure 4 | *In situ* TEM observation of graphene cage Si lithiation. a**, Diagram of the nanoscale electrochemical cell for *in situ* (de)lithiation within the TEM. **b**, Time-lapse images of the lithiation of graphene-encapsulated SiMP (Supplementary Video 3). The Si microparticle (outlined in red) fractures abruptly and violently within the mechanically strong graphene cage (outlined in black), which remains intact throughout the highly anisotropic process.

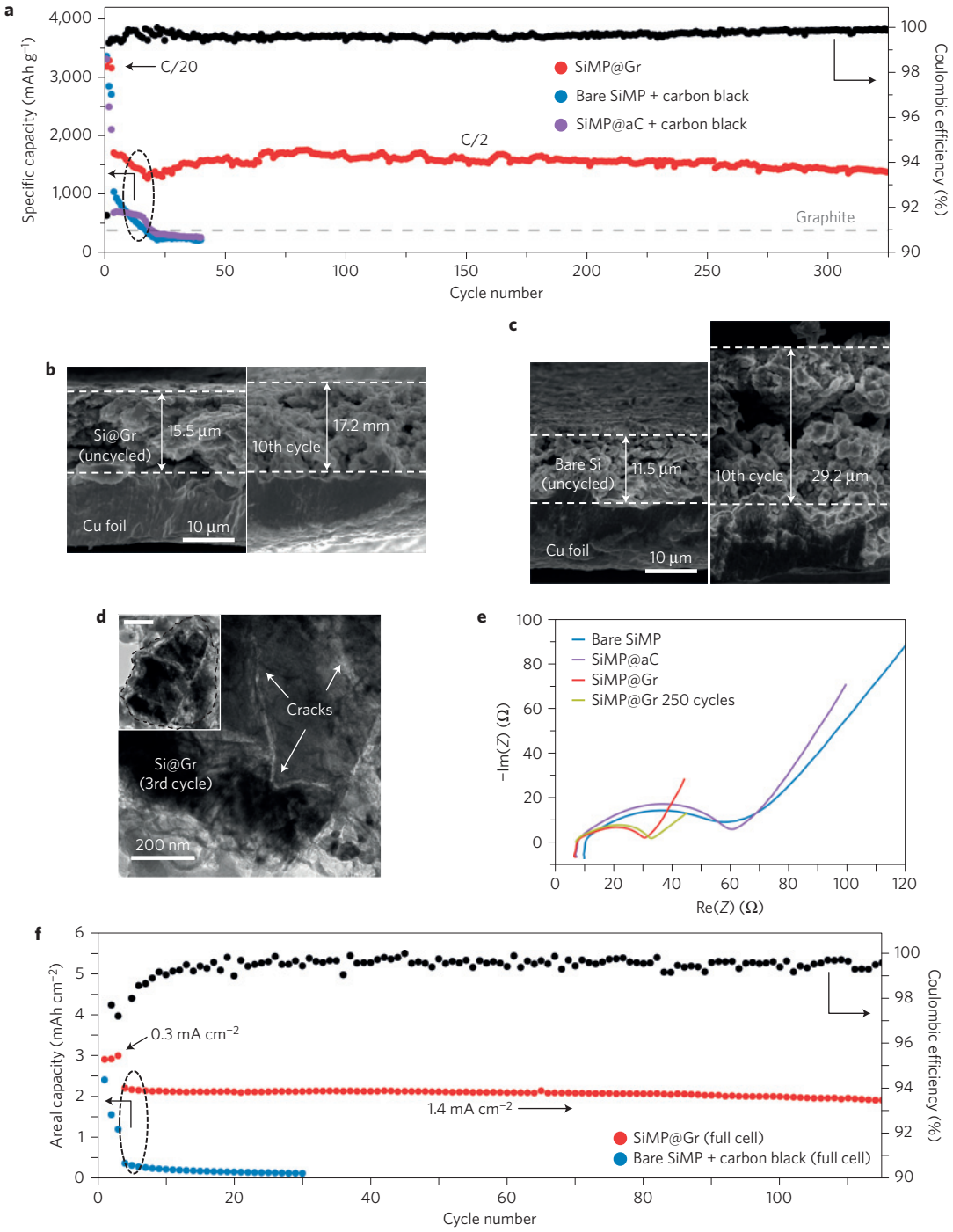


**Figure 5 | Electrochemical characterization of graphene cage Si anodes.** All specific capacities are reported based on the total mass of the active materials (Si and C). **a**, Half-cell delithiation capacity of SiMP@Gr with no conductive additives. Bare and amorphous-carbon-coated SiMP are control samples with carbon black conductive additives. The mass loading of all active materials was ~0.8 mg cm$^{-2}$. The rate was C/20 for the initial three cycles and C/2 (1.5 mA cm$^{-2}$) for later cycles (1C = 4.2 A g$^{-1}$ Si). The theoretical capacity (370 mAh g$^{-1}$) of a graphite electrode is shown as a grey dashed line. The Coulombic efficiency of the SiMP@Gr is plotted on the secondary *y*-axis. **b**,**c**, Cross-sectional SEM images of graphene-encapsulated (**b**) and bare (**c**) SiMP electrodes before (left) and after (right) cycling. **d**, *Ex situ* TEM image of graphene-encapsulated SiMP after three cycles. White arrows indicate particle fracture is confined within the graphene cage. Inset shows graphene cage (outlined in black) remains fully intact. **e**, EIS measurements of graphene-encapsulated, bare and amorphous-carbon-coated SiMP. Note that the graphene cage exhibits faster surface kinetics than bare and amorphous-carbon-coated SiMP, with no observable change even after 250 cycles. **f**, Full-cell delithiation capacity of SiMP@Gr (~2.0 mg) with no conductive additives paired with a traditional lithium cobalt oxide cathode. The Coulombic efficiency of the SiMP@Gr is plotted on the secondary *y*-axis.

consumption during SEI formation. As can be seen in typical voltage profiles and compiled coin cell statistics (Supplementary Figs 8 and 9), the initial-cycle Coulombic efficiency for bare SiMP is only 83%. This value drops considerably for an amorphous carbon coating (74%) owing to the large number of dangling carbon bonds acting as Li-trapping sites. Furthermore, even the best performing nano-Si anodes typically takes many cycles for the Coulombic efficiency to reach above 99%. In comparison,

the graphene-encapsulated SiMP exhibits initial-cycle Coulombic efficiencies as high as 93.2% (Supplementary Fig. 9) and quickly increases to 99.5% within the first five cycles (Fig. 5a). After only ten cycles, it reaches 99.9%. For comparison, the first-cycle Coulombic efficiency in commercial graphite anodes is ~90–94%, jumping to 99.9% in the early cycles[46].

The improvement in early- and later-cycle Coulombic efficiency can be explained in terms of two requirements met by the graphene cage design: the surface chemistry must allow initial SEI formation without consuming too much Li, and the interface with electrolyte must be mechanically stable to prevent additional SEI formation. First, the layered morphology (Fig. 2d) of the conformal graphene cage is structurally and chemically similar to that of graphite, making the graphitized carbon atoms of the cage unlikely to trap Li. Furthermore, the use of micrometre-sized Si (Supplementary Fig. 3) lowers the surface area accessible by the electrolyte and thus minimizes possible side reactions. Despite possible defects in the graphene cage, our results show that the graphite-like surface and low surface area of the microscale Si allows the composite to reach an initial-cycle Coulombic efficiency approaching that of graphite. Second, the mechanically stable graphene cage prevents uncontrolled SEI formation. This is supported by the Nyquist plot obtained from electrochemical impedance spectroscopy (EIS), where the semicircle represents the charge-transfer resistance. Not only are the surface kinetics of the graphene-encapsulated SiMP much faster than that of the bare or amorphous-carbon-coated SiMP, but this behaviour also remains largely unchanged even after 250 cycles (Fig. 5e). Along with a 99.9% Coulombic efficiency in later cycles (Fig. 5a), the EIS data provide strong evidence for a stable SEI layer during cycling of the graphene-encapsulated SiMP.

Both criteria for high Coulombic efficiencies are met by commercial graphite anodes, enabling their excellent battery performance in full cells. Full-cell demonstrations of the Si anode have largely been avoided in the past owing to the rigorous requirements demanded of the electrode materials. In contrast to the nearly unlimited Li supply in half cells, full cells have a finite source of Li ions. Low Coulombic efficiencies in the early cycles irreversibly consume Li ions, thus leading to severe battery decay. Therefore, reaching high Coulombic efficiency in the early cycles is critical to achieving stable cycling in a full cell. Furthermore, electrode materials with high mass loadings are necessary for practical full-cell demonstrations, but place a much heavier burden on cycling stability (see discussion in Supplementary Information).

The graphene cage maintains electrical connectivity of the fractured Si on both the particle and electrode level, while simultaneously reaching high Coulombic efficiencies very rapidly. Thus, we are able to construct a practical full-cell battery with high mass and improved cycling performance (Fig. 5f). When paired with a traditional lithium cobalt oxide (LCO) cathode, the graphene-encapsulated SiMP exhibits stable cycling (100 cycles, 90% capacity retention) and high Coulombic efficiency (99.6% average after the fifth cycle) at practical values of current density (1.4 mA $cm^{-2}$) and areal capacity (3.1 mAh $cm^{-2}$). Furthermore, the voltage profiles at various cycle numbers (Supplementary Fig. 14) show no increase in the overpotential—another indication that both electrodes, as well as their interfaces, are stable during cycling. This unprecedented full-cell stability for a material never before shown to cycle well (even in half-cell configurations) demonstrates the power of our graphene cage approach. The combined mechanical, electrical and chemical properties of the graphene cage allow us to fulfil the most stringent requirements thus far demanded of the Si anode material.

## Conclusion

We emphasize that our graphene cage concept is fundamentally different from previous reports of graphene coatings[26,47–50]. Instead of relying on physical mixing or chemical vapour deposition of Si in graphene flakes for an incomplete and nonconformal graphene coverage on nano-Si, we are able to grow the graphene cage directly onto micro-Si in a conformal manner. Moreover, our versatile strategy is successful for Si microparticles with extremely non-uniform distributions of size and shape (Supplementary Fig. 1). This results in a highly conformal graphene cage with a built-in and tunable void space. The graphene cage concept introduced here is also different from a recently reported coating strategy[26] based on the following two aspects: the successful stabilization of fracture-prone micrometre-sized Si particles; a tunable void space coupled with highly graphitic carbon to rapidly improve SEI stability and Coulombic efficiency.

We have established an innovative and facile synthesis approach to encapsulate Si with a unique graphene cage structure that exhibits a suite of attractive properties. Our materials design fulfils the most rigorous requirements demanded of Si thus far: maintaining electrical connectivity of fractured particles while simultaneously attaining the high Coulombic efficiencies needed for full-cell operation. As a result, two long-standing issues with microscale Si have been resolved: particle fracture and SEI stability. Without making use of any conductive additives, the graphene-encapsulated SiMP has achieved stable cycling in a full cell for the first time. This strategy can also be expanded to include a wide range of other materials that fail in electrochemical reactions. By imparting mechanical strength, electrical conductivity and chemical stability, encapsulation by a graphene cage demonstrates a powerful new method to address failure modes in electrodes, making energy-dense, low-cost battery materials a realistic possibility.

## Methods

**Synthesis of graphene-encapsulated Si microparticles.** The surface of Si must be densely coated with a nucleation seed (Pd in this case) for a conformal Ni coating. Simply, we used polydopamine (~3 nm) as a surface-adherent layer to sensitize the Si surface with Sn(II) ions, which subsequently reduced the Pd metal seed from solution onto Si.

In a typical synthesis, ~2 g SiMP (1–3 μm; US Research Nanomaterials) was dispersed in 160 ml of deionized (DI) water and sonicated for ~10 min. 1.6 ml of Tris-buffer (1.0 M; pH 8.5; Teknova) and 320 mg dopamine hydrochloride (Sigma-Aldrich) were sequentially added to the aqueous solution and stirred at room temperature for 1 h. This formed a very thin layer of polydopamine that helped the Ni-nucleation seed adhere more readily to the Si surface[51]. Next, 20 ml of stannous chloride aqueous solution (5 g $l^{-1}$ $SnCl_2$; 10 ml $l^{-1}$ hydrochloric acid (HCl); Sigma-Aldrich) was directly added to the mixture and stirred for an additional 1 h. The decrease in pH prevents the polydopamine layer from growing thicker. The sample was then collected by centrifugation and washed three times with DI water. Finally, the particles were immersed in 30 ml of palladium chloride aqueous solution (0.5 g $l^{-1}$ $PdCl_2$; 6.25 ml $l^{-1}$ HCl; Sigma-Aldrich) and stirred for 1 h. Washing three times with DI water and collecting by centrifugation resulted in activated SiMP.

The thickness of the Ni coating can be tuned either by changing the concentration of the electroless Ni (EN) solution or controlling the number of deposition reactions. In our case, we used a combination of both approaches. Two electroless Ni solutions were prepared: a primary solution (20 g $l^{-1}$ nickel sulphate hexahydrate; 10 g $l^{-1}$ sodium citrate dihydrate; 5 g $l^{-1}$ lactic acid) and a secondary solution with double the component concentration (40 g $l^{-1}$ nickel sulphate hexahydrate; 20 g $l^{-1}$ sodium citrate dihydrate; 10 g $l^{-1}$ lactic acid). Activated SiMP was sequentially immersed in these EN solutions.

Before the first electroless deposition, 1 g of dimethylamine borane (DMAB; Sigma-Aldrich) and 2 ml of ammonium hydroxide ($NH_3 \cdot H_2O$, Sigma-Aldrich, 28%) were added to 180 ml of the primary EN solution. The pH-sensitive DMAB served as the reducing agent during electroless Ni deposition. 500 mg of activated SiMP was then added to the dilute EN solution and gently stirred for ~30 min. Bubbles began to effervesce and the green-coloured EN solution became lighter in colour as the reaction proceeded. After deposition was complete, the SiMP@1xNi settled to the bottom. While holding the SiMP@1xNi particles at the bottom of the container with a magnet, the depleted EN bath was carefully poured out. In a separate container, 2 g of DMAB and 3 ml of ammonium hydroxide were added to 180 ml of the secondary EN solution. This was then added immediately to the damp particles (SiMP@1xNi) and stirred for ~30 min. The resulting SiMP@2xNi was washed twice with ethanol and dried in a vacuum oven at 50 °C for 1 h.

We dispersed dried SiMP@2xNi (~2.3 g after EN) in 150 ml of triethylene glycol (Santa Cruz Biotechnology) and 500 μl of 50% w/w aqueous NaOH

solution. After stirring at 185 °C for ~8 h, the carburized SiMP@2xNi was collected by centrifugation and washed three times with ethanol. The carburization process occurred when the organic solvent decomposed, allowing carbon atoms to diffuse into the Ni layer and adhere to the surface. This primes the SiMP@2xNi for low-temperature graphene growth. Samples were then dried in a vacuum oven at 50 °C for 1 h. The dried particles were placed in a tube furnace with the following temperature profile: heat to 100 °C at 2 °C $min^{-1}$; heat to 450 °C at 20 °C $min^{-1}$; hold temperature at 450 °C for 1 h. An Ar flow rate of 80 sccm was maintained throughout the annealing process. The dual-purpose Ni template and native oxide layer on Si were etched by sequentially immersing the annealed particles in 1 M $FeCl_3$ (2 h) and 10 vol% hydrogen fluoride aqueous solution (30 min), respectively. Graphene-encapsulated SiMP were obtained (~400 mg) after washing three times with ethanol and drying in a vacuum oven at 50 °C for 1 h (Supplementary Fig. 3).

**Synthesis of amorphous-carbon-coated Si microparticles.** 500 mg of SiMP was dispersed in 120 ml water. 4 ml of Cetrimonium bromide (CTAB, Sigma-Aldrich, 10 mM) and 0.4 ml ammonia were added and the solution was stirred for 20 min to ensure the adsorption of CTAB on the silicon surface. Next, 100 mg resorcinol (Sigma-Aldrich) and 140 µl formaldehyde solution (Sigma-Aldrich, 37% wt% in $H_2O$) were added and stirred overnight[52,53]. The final RF-coated Si was collected by centrifugation and washed with ethanol three times. The RF shell was carbonized under Ar at 800 °C for 2 h with a heating rate of °C $min^{-1}$.

***In situ* TEM.** A piezo-controlled, electrical biasing TEM-AFM holder (Nanofactory Instruments) was used to observe the (de)lithiation process of graphene-encapsulated SiMP and measure the graphene cage's electrical and mechanical properties. Li metal and SiMP@Gr were dispersed onto 0.25 mm W and Cu wires, respectively. They were then brought into contact by the piezo-controller. By applying a voltage bias of −3 V, Li ions flowed through the Li metal's native oxide/nitride to alloy with Si at the working electrode. The graphene cage remained intact despite the violent anisotropic fracture of the SiMP. To determine the graphene cage's current–voltage behaviour, SiMP@Gr was dropcast onto a 0.25 mm Au wire. A bare W wire with a sharp tip was used to contact the graphene cage, completing the circuit. Measuring current as a function of applied voltage confirmed that the graphene cage was over two orders of magnitude more electrically conductive than amorphous carbon. Not only does this obviate the need for conductive additives in electrochemical cells, it also affords excellent rate performance (Supplementary Fig. 11). For external load testing, the piezo-controller was used to push the W tip into the graphene cage. The reversible deformation makes it a suitable encapsulation material for anisotropic SiMP expansion and fracture.

**Electrochemistry.** Working electrodes for cycling stability (Fig. 5a and Supplementary Fig. 10), rate capability (Supplementary Fig. 11), and high areal capacity (Supplementary Fig. 12) tests were all prepared using a conventional slurry method. SiMP@Gr powders and polyvinylidene fluoride (PVDF, Kynar HSV 900) binder with a mass ratio of 9:1 were dispersed in *N*-methyl-2-pyrrolidone (NMP) in the absence of any conductive additives and stirred for 12 h. Control electrodes with bare SiMP or SiMP@aC were prepared using the same slurry method, except using a mass ratio of 8:1:1 for active material, carbon black conductive additive (Super P, TIMCAL, Switzerland), and PVDF-binder, respectively. After casting onto a 15-µm-thick Cu foil and drying at 50 °C in a vacuum oven for 3 h, the samples were calendered and cut into 1 $cm^2$ circular disks with a mass loading of ~0.8–2.5 mg $cm^{-2}$. For calendering, the cast electrode was sandwiched between two Cu foils and placed into a hand-crank calendering machine. Although the exact pressure was not displayed on the machine, the thickness of the SiMP@Gr cast onto the Cu foil changed from ~50 µm before calendering to ~15 µm after calendering. In an Ar-filled glovebox, these working electrodes were assembled into type 2032 coin cells with a polymer separator (Celgard 2250) and Li metal (Alfa Aesar) as the counter/reference electrode (half cell) or lithium cobalt oxide (LCO) as the cathode (full cell). 100 µl of 1.0 M $LiPF_6$ in 89 vol% 1:1 w/w ethylene carbonate/diethyl carbonate (BASF Selectilyte LP40) with 10 vol% fluoroethylene carbonate and 1 vol% vinylene carbonate (Novolyte Technologies) was added as the electrolyte with full wetting of both working and counter electrode surfaces. For experiments with no electrolyte additive, see Supplementary Fig. 13. Coin cells were loaded into a battery test (Arbin Instruments) and cycled between 0.01 and 1 V (half cell) or 3.0–4.2 V (full cell). The mass loading of the Si@Gr electrode (~11 mm diameter) in a full-cell configuration was ~2.0 mg $cm^{-2}$, giving an areal capacity of ~4.5 mAh $cm^{-2}$ at a current density of 0.3 mA $cm^{-2}$ when Li metal was used as the counter electrode. The areal capacity of the LCO cathode (~9.5 mm diameter) tested with Li metal as the counter electrode was ~4.0 mAh $cm^{-2}$ at a current density of 0.3 mA $cm^{-2}$, giving a theoretical N/P ratio of ~1.13. The Si anode in the full cell was prepared exactly as described for our half-cell experiments and did not undergo any pre-cycling or pre-lithiation before being used in the full cell. The specific capacity for all cells was calculated using the total mass of the graphene-encapsulated SiMP composite. Charge/discharge rates were calculated assuming silicon's theoretical capacity (4,200 mAh $g^{-1}$ Si). Coulombic efficiency was calculated using the ratio of delithiation ($C_{dealloy}$) capacity to lithiation ($C_{alloy}$) capacity ($C_{dealloy}/C_{alloy} \times 100\%$).

For *ex situ* SEM/TEM characterization of working electrodes, coin cells were charged to 1 V and disassembled. The working electrodes were then rinsed gently in acetonitrile to remove Li salts from the residual electrolyte.

Received 29 September 2015; accepted 22 December 2015; published 25 January 2016

## References


1. Aricò, A. S., Bruce, P., Scrosati, B., Tarascon, J.-M. & van Schalkwijk, W. Nanostructured materials for advanced energy conversion and storage devices. *Nature Mater.* **4**, 366–377 (2005).
2. Armand, M. & Tarascon, J.-M. Building better batteries. *Nature* **451**, 652–657 (2008).
3. Bruce, P. G., Freunberger, S. A., Hardwick, L. J. & Tarascon, J.-M. Li–$O_2$ and Li–S batteries with high energy storage. *Nature Mater.* **11**, 19–29 (2012).
4. Chan, C. K. *et al.* High-performance lithium battery anodes using silicon nanowires. *Nature Nanotech.* **3**, 31–35 (2008).
5. Yang, S., Zavalij, P. Y. & Whittingham, M. S. Anodes for lithium batteries: tin revisited. *Electrochem. Commun.* **5**, 587–590 (2003).
6. Zheng, G. *et al.* Interconnected hollow carbon nanospheres for stable lithium metal anodes. *Nature Nanotech.* **9**, 618–623 (2014).
7. Qian, J. *et al.* High rate and stable cycling of lithium metal anode. *Nature Commun.* **6**, 6362 (2015).
8. Ogasawara, T., Débart, A., Holzapfel, M., Novák, P. & Bruce, P. G. Rechargeable $Li_2O_2$ electrode for lithium batteries. *J. Am. Chem. Soc.* **128**, 1390–1393 (2006).
9. Ji, X., Lee, K. T. & Nazar, L. F. A highly ordered nanostructured carbon–sulphur cathode for lithium–sulphur batteries. *Nature Mater.* **8**, 500–506 (2009).
10. Lu, Y.-C., Gasteiger, H. A., Crumlin, E., McGuire, R. & Shao-Horn, Y. Electrocatalytic activity studies of select metal surfaces and implications in Li–air batteries. *J. Electrochem. Soc.* **157**, A1025 (2010).
11. Seh, Z. W. *et al.* Sulphur–$TiO_2$ yolk–shell nanoarchitecture with internal void space for long-cycle lithium–sulphur batteries. *Nature Commun.* **4**, 1331 (2013).
12. Beaulieu, L. Y., Eberman, K. W., Turner, R. L., Krause, L. J. & Dahn, J. R. Colossal reversible volume changes in lithium alloys. *Electrochem. Solid-State Lett.* **4**, A137–A140 (2001).
13. Obrovac, M. N. & Christensen, L. Structural changes in silicon anodes during lithium insertion/extraction. *Electrochem. Solid-State Lett.* **7**, A93–A96 (2004).
14. Obrovac, M. N., Christensen, L., Le, D. B. & Dahn, J. R. Alloy design for lithium-ion battery anodes. *J. Electrochem. Soc.* **154**, A849–A855 (2007).
15. Cui, L.-F., Ruffo, R., Chan, C. K., Peng, H. & Cui, Y. Crystalline-amorphous core–shell silicon nanowires for high capacity and high current battery electrodes. *Nano Lett.* **9**, 491–495 (2008).
16. Zhou, S., Liu, X. & Wang, D. Si/TiSi2 heteronanostructures as high-capacity anode material for Li ion batteries. *Nano Lett.* **10**, 860–863 (2010).
17. Yao, Y. *et al.* Interconnected silicon hollow nanospheres for lithium-ion battery anodes with long cycle life. *Nano Lett.* **11**, 2949–2954 (2011).
18. Park, M.-H. *et al.* Silicon nanotube battery anodes. *Nano Lett.* **9**, 3844–3847 (2009).
19. Xiao, J. *et al.* Stabilization of silicon anode for Li-ion batteries. *J. Electrochem. Soc.* **157**, A1047–A1051 (2010).
20. Yi, R., Dai, F., Gordin, M. L., Chen, S. & Wang, D. Micro-sized Si–C composite with interconnected nanoscale building blocks as high-performance anodes for practical application in lithium-ion batteries. *Adv. Energy Mater.* **3**, 295–300 (2013).
21. Ge, M., Rong, J., Fang, X. & Zhou, C. Porous doped silicon nanowires for lithium ion battery anode with long cycle life. *Nano Lett.* **12**, 2318–2323 (2012).
22. Lu, Z. *et al.* Nonfilling carbon coating of porous silicon micrometer-sized particles for high-performance lithium battery anodes. *ACS Nano* **9**, 2540–2547 (2015).
23. Magasinski, A. *et al.* High-performance lithium-ion anodes using a hierarchical bottom-up approach. *Nature Mater.* **9**, 353–358 (2010).
24. Ji, L. *et al.* Graphene/Si multilayer structure anodes for advanced half and full lithium-ion cells. *Nano Energy* **1**, 164–171 (2012).
25. Ren, J. *et al.* Silicon–graphene composite anodes for high-energy lithium batteries. *Energy Technol.* **1**, 77–84 (2013).
26. Son, I. H. *et al.* Silicon carbide-free graphene growth on silicon for lithium-ion battery with high volumetric energy density. *Nature Commun.* **6**, 7393 (2015).
27. Wu, H. *et al.* Stable cycling of double-walled silicon nanotube battery anodes through solid-electrolyte interphase control. *Nature Nanotech.* **7**, 310–315 (2012).

28. Liu, N. *et al.* A yolk-shell design for stabilized and scalable Li-ion battery alloy anodes. *Nano Lett.* **12**, 3315–3321 (2012).
29. Liu, N. *et al.* A pomegranate-inspired nanoscale design for large-volume-change lithium battery anodes. *Nature Nanotech.* **9**, 187–192 (2014).
30. Kovalenko, I. *et al.* A major constituent of brown algae for use in high-capacity Li-ion batteries. *Science* **334**, 75–79 (2011).
31. Wu, H. *et al.* Stable Li-ion battery anodes by *in-situ* polymerization of conducting hydrogel to conformally coat silicon nanoparticles. *Nature Commun.* **4**, 1943 (2013).
32. Wang, C. *et al.* Self-healing chemistry enables the stable operation of silicon microparticle anodes for high-energy lithium-ion batteries. *Nature Chem.* **5**, 1042–1048 (2013).
33. Kim, H., Seo, M., Park, M. & Cho, J. A critical size of silicon nano-anodes for lithium rechargeable batteries. *Angew. Chem. Int. Ed.* **49**, 2146–2149 (2010).
34. Lee, S. W., McDowell, M. T., Choi, J. W. & Cui, Y. Anomalous shape changes of silicon nanopillars by electrochemical lithiation. *Nano Lett.* **11**, 3034–3039 (2011).
35. Liu, X. H. *et al.* Anisotropic swelling and fracture of silicon nanowires during lithiation. *Nano Lett.* **11**, 3312–3318 (2011).
36. McMillan, R., Slegr, H., Shu, Z. X. & Wang, W. Fluoroethylene carbonate electrolyte and its use in lithium ion batteries with graphite anodes. *J. Power Sources* **81–82**, 20–26 (1999).
37. Profatilova, I. A., Kim, S.-S. & Choi, N.-S. Enhanced thermal properties of the solid electrolyte interphase formed on graphite in an electrolyte with fluoroethylene carbonate. *Electrochim. Acta* **54**, 4445–4450 (2009).
38. Jeong, S.-K. *et al.* Surface film formation on a graphite negative electrode in lithium-ion batteries: atomic force microscopy study on the effects of film-forming additives in propylene carbonate solutions. *Langmuir* **17**, 8281–8286 (2001).
39. Schlesinger, M. & Paunovic, M. *Modern Electroplating* Vol. 55 (Wiley, 2011).
40. Nagakura, S. Study of metallic carbides by electron diffraction part I. Formation and decomposition of nickel carbide. *J. Phys. Soc. Jpn* **12**, 482–494 (1957).
41. Yoon, S.-M. *et al.* Synthesis of multilayer graphene balls by carbon segregation from nickel nanoparticles. *ACS Nano* **6**, 6803–6811 (2012).
42. Li, X., Cai, W., Colombo, L. & Ruoff, R. S. Evolution of graphene growth on Ni and Cu by carbon isotope labeling. *Nano Lett.* **9**, 4268–4272 (2009).
43. Ferrari, A. C. & Robertson, J. Interpretation of Raman spectra of disordered and amorphous carbon. *Phys. Rev. B* **61**, 14095–14107 (2000).
44. Huang, J. Y. *et al. In situ* observation of the electrochemical lithiation of a single $SnO_2$ nanowire electrode. *Science* **330**, 1515–1520 (2010).
45. McDowell, M. T. *et al. In situ* TEM of two-phase lithiation of amorphous silicon nanospheres. *Nano Lett.* **13**, 758–764 (2013).
46. Smith, A. J., Burns, J. C., Trussler, S. & Dahn, J. R. Precision measurements of the coulombic efficiency of lithium-ion batteries and of electrode materials for lithium-ion batteries. *J. Electrochem. Soc.* **157**, A196–A202 (2010).
47. Chou, S.-L. *et al.* Enhanced reversible lithium storage in a nanosize silicon/graphene composite. *Electrochem. Commun.* **12**, 303–306 (2010).
48. Xiang, H. *et al.* Graphene/nanosized silicon composites for lithium battery anodes with improved cycling stability. *Carbon* **49**, 1787–1796 (2011).
49. Zhou, X., Yin, Y., Wan, L. & Guo, Y. Self-assembled nanocomposite of silicon nanoparticles encapsulated in graphene through electrostatic attraction for lithium-ion batteries. *Adv. Energy Mater.* **2**, 1086–1090 (2012).
50. Luo, J. *et al.* Crumpled graphene-encapsulated Si nanoparticles for lithium ion battery anodes. *J. Phys. Chem. Lett.* **3**, 1824–1829 (2012).
51. Lee, H., Dellatore, S. M., Miller, W. M. & Messersmith, P. B. Mussel-inspired surface chemistry for multifunctional coatings. *Science* **318**, 426–430 (2007).
52. Liu, J. *et al.* Extension of the Stöber Method to the preparation of monodisperse resorcinol–formaldehyde resin polymer and carbon spheres. *Angew. Chem. Int. Ed.* **50**, 5947–5951 (2011).
53. Li, N. *et al.* Sol–gel coating of inorganic nanostructures with resorcinol–formaldehyde resin. *Chem. Commun.* **49**, 5135–5137 (2013).


## Acknowledgements

Y.L. acknowledges the National Science Foundation Graduate Fellowship Program for funding and M. Hanna for fruitful discussions. H.-W.L. acknowledges the Basic Science Research Program through the National Research Foundation of Korea (NRF) funded by the Ministry of Education, Science and Technology (contract no. 2012038593). Y.C. acknowledges the support from the Assistant Secretary for Energy Efficiency and Renewable Energy, Office of Vehicle Technologies of the US Department of Energy under the Battery Materials Research (BMR) Program.

## Author contributions

Y.L., K.Y. and Y.C. conceived and designed the experiments. Y.L. and K.Y. carried out materials synthesis and electrochemical characterization. Z.L. and N.L. participated in part of the synthesis and materials characterization. H.-W.L. and Y.L. conducted *in situ* TEM lithiation and electrical measurements. Y.L., K.Y. and Y.C. co-wrote the paper. All authors discussed the results and commented on the manuscript.

## Additional information

Supplementary information is available online. Reprints and permissions information is available online at www.nature.com/reprints. Correspondence and requests for materials should be addressed to Y.C.

## Competing interests

The authors declare no competing financial interests.